

Nutrient levels and trade-offs control diversity in a model seasonal ecosystem

Amir Erez,^{1,*} Jaime G. Lopez,^{2,*} Benjamin Weiner,³ Yigal Meir,⁴ and Ned S. Wingreen^{1,2,†}

¹*Department of Molecular Biology, Princeton University, Princeton, New Jersey 08544, USA*

²*Lewis-Sigler Institute for Integrative Genomics, Princeton University, Princeton, New Jersey 08544, USA*

³*Department of Physics, Princeton University, Princeton, New Jersey 08544, USA*

⁴*Department of Physics, Ben Gurion University of the Negev, Beer Sheva, Israel*

(Dated: May 10, 2022)

Microbial communities feature an immense diversity of species and the extent of this diversity correlates with outcomes ranging from ecosystem stability to medical prognoses. Yet the mechanisms underlying microbial diversity are not well understood; simple resource-competition models do not allow for coexistence of a large number of species. However, it was recently shown that metabolic trade-offs can lead to unlimited diversity in a chemostat model. Do such trade-offs permit diversity under more realistic, intermittent conditions of nutrient supply? Here, we demonstrate that in serial dilution culture, metabolic trade-offs allow for high diversity. Unlike the chemostat case, diversity depends on the amount of nutrient supplied to the community. The form of this dependence varies with the precision of trade-offs and the presence of cross-feeding, immigration, or evolution. The large variation seen in this simple model suggests that real ecosystems may not obey a single universal relationship between nutrient supply and diversity. To connect to real microbial communities, we validate our model framework against previously published *Escherichia coli* batch and chemostat experiments and outline potential future experiments to test the model’s multispecies predictions.

Keywords: Microbial diversity | Resource-competition model | Serial dilution | Competitive exclusion

Introduction

Microbial communities feature an immense diversity of organisms, with the typical human gut microbiota containing hundreds, and a gram of soil containing thousands, of distinct microbial genomes [1, 2]. These observations clash with a prediction of resource-competition models, known as the competitive-exclusion principle – namely, that steady-state coexistence is possible for only as many species as resources [3, 4]. This conundrum is familiarly known as the “paradox of the plankton” [5]. Solving this paradox may provide one key to predicting and controlling outcomes ranging from ecosystem stability to successful cancer treatments in humans [6–9]. Many possible solutions of the paradox have been offered: (i) interactions between microbes, such as cross-feeding or antibiotic production and degradation [10, 11], (ii) spatial heterogeneity [12, 13], (iii) persistent non-steady-state dynamics [5], and (iv) predation by viruses [14]. Many explanations for the paradox commonly assume a chemostat framework wherein nutrients are continuously supplied and there is a continuous removal of biomass and unused nutrients [15]. However, in nature nutrients are rarely supplied in a constant and continuous fashion. In particular, seasonal variation is ubiquitous in ecology, influencing systems ranging from oceanic phytoplankton communities [16] to the microbiota of some human populations [17]. How does a variable nutrient supply influence diversity?

To address this question, we consider a known resource-competition model that permits high diversity at steady state due to metabolic trade-offs, but now in the context of serial dilution to reflect a more realistic variable nutrient sup-

ply. Serial dilution is well-established as an experimental approach. For example, the bacterial populations in the Lenski long-term evolution experiment [18], experiments on community assembly [19], and antibiotic cross-protection [20] were all performed in serial dilution. While previous models of serial dilution have characterized competition between small numbers of species with trade-offs in their growth characteristics [21, 22], the theoretical understanding of diversity in serial dilution is much less developed than for chemostat-based steady-state growth.

Here, we show that metabolic trade-offs allow a serial dilution system to support unlimited coexistence, but that, unlike the chemostat case, community diversity depends upon both nutrient bolus and inoculum size. This dependence allowed us to explore an unresolved question in ecology [23–25]: what is the relationship between the amount of nutrient supplied and the resulting diversity of the community? Experimental studies of this question have mainly been performed in macroecological contexts [26–28], though recently there has been increased focus on microbial systems [29, 30]. In microbial experiments, some evidence has supported the “hump-shaped” unimodal trend predicted by many theories [31]. However, a meta-analysis by Smith [32] found no consistent trend across microbial experiments. What we observe here is concordant with Smith’s result: even in our highly simplified model, there is no general relationship between nutrient supply and diversity. Among the factors we find that influence this relationship are cross-feeding, relative enzyme budgets, and the presence of mutation. That so much variation appears in a simple model suggests that real ecosystems are not likely to display a single universal relationship between nutrient supply and diversity. To connect to real microbial systems, we then compare our model framework of substitutable and simultaneous nutrient consumption to previously published experimental data from *Escherichia coli* growing in batch and chemostat conditions. We find that our model agrees quantitatively with both

*These authors contributed equally, listed alphabetically

†Corresponding author, email: wingreen@princeton.edu

datasets and outline potential future experiments to test the model’s multispecies predictions.

Results

We employ the serial dilution model depicted in Fig. 1A. At the beginning of each batch ($t = 0$), we introduce the inoculum, defined as a collection of species $\{\sigma\}$ with initial biomass densities $\rho_\sigma(0)$ in the batch such that the total initial biomass density is $\rho_0 = \sum_\sigma \rho_\sigma(0)$. Together with the inoculum, we supply a nutrient bolus, defined as a mixture of p nutrients each with concentration in the batch $c_i(0)$, $i = 1, \dots, p$ such that the total nutrient concentration is $c_0 = \sum_{i=1}^p c_i(0)$. For simplicity, we assume ideal nutrient to biomass conversion, so that for a species to grow one unit of biomass density, it consumes one unit of nutrient concentration – this can be viewed as a choice of the nutrient units (we consider the case of nutrient-specific yields Y_i in *Appendix Fig. 8* and show it does not qualitatively alter coexistence in the model). During each batch, the species biomass densities $\rho_\sigma(t)$ increase with time, starting at $t = 0$, and growth continues until the nutrients are fully depleted, $\sum_{i=1}^p c_i(\infty) \approx 0$. Thus, at the end of a batch, the total biomass density of cells is $\sum_\sigma \rho_\sigma(\infty) = \rho_0 + c_0$. The next batch is then inoculated with a biomass density ρ_0 with a composition that reflects the relative abundance of each species in the total biomass at the end of the previous batch. This process is repeated until “steady state” is reached, i.e. when the biomass composition at the beginning of each batch stops changing.

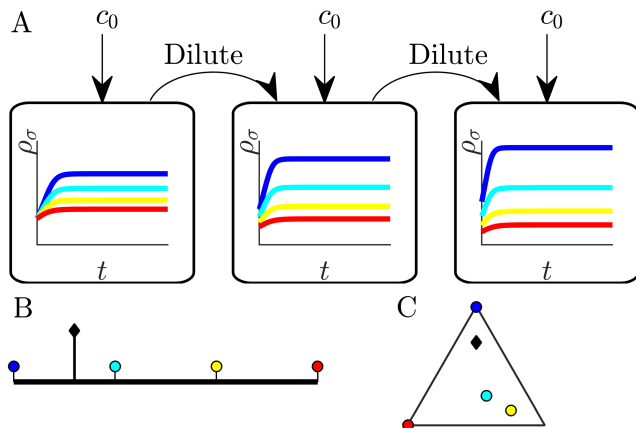


FIG. 1: Illustration of serial dilution resource-competition model. (A) Serial dilution protocol. Each cycle of batch growth begins with a cellular biomass density ρ_0 and total nutrient concentration c_0 . The system evolves according to Eqs. 2-3 until nutrients are completely consumed. A sample of the total biomass is then used to inoculate the next batch again at density ρ_0 . (B) Representation of particular enzyme-allocation strategies $\{\alpha_\sigma\}$ (colored circles) and nutrient supply composition c_i/c_0 (black diamond) on a 2-nutrient simplex, where the right endpoint corresponds to 100% Nutrient 1. (C) Representation of particular strategies (circles) and nutrient supply (black diamond) on a 3-nutrient simplex.

In the model, a species σ is defined by its unique enzyme strategy $\vec{\alpha}_\sigma = (\alpha_{\sigma,i}, \dots, \alpha_{\sigma,p})$ which determines its ability to consume different nutrients. Each species can consume multiple nutrients simultaneously, in line with the behavior of microbes at low nutrient concentrations [33]. Specifically, we assume that species σ consumes nutrient i at a rate $j_{\sigma,i}$ (per unit biomass) that depends on nutrient availability c_i and on its enzyme allocation strategy $\alpha_{\sigma,i}$ according to

$$j_{\sigma,i} = \frac{c_i}{K_i + c_i} \alpha_{\sigma,i}. \quad (1)$$

For simplicity, we take all Monod constants to be equal, $K_i = K$ (a more general form of the nutrient model is considered in *Appendix B*). During each batch, the dynamics of nutrient concentrations and biomass densities then follow from the rates $j_{\sigma,i}$ at which the species consume nutrients:

$$\frac{dc_i}{dt} = - \sum_\sigma \rho_\sigma j_{\sigma,i}, \quad (2)$$

$$\frac{d\rho_\sigma}{dt} = \rho_\sigma \sum_i j_{\sigma,i}. \quad (3)$$

Since the level of one enzyme inevitably comes at the expense of another, we model this trade-off via an approximately fixed total enzyme budget E . Formally, we take $\sum_i \alpha_{\sigma,i} = E + \varepsilon \xi_\sigma$, where ξ_σ is a zero-mean and unit-variance Gaussian variable. Without loss of generality we take $E = 1$; initially we set $\varepsilon = 0$. This allows us to visualize the strategies $\vec{\alpha}_\sigma$ as points on a simplex, depicted as colored circles embedded in: (i) the interval $[0, 1]$ for two nutrients (Fig. 1B), or (ii) a triangle for three nutrients (Fig. 1C). One can plot the nutrient bolus composition c_i/c_0 on the same simplex, as depicted by the black diamonds in Fig. 1B and C. In what follows, we focus on the case of two nutrients, though the main results extend to an arbitrarily large number of nutrients.

One can intuit that our serial dilution model at very low nutrient bolus size will mimic a chemostat. Adding a small nutrient bolus, letting it be consumed, then removing the additional biomass, and repeating is tantamount to operating a chemostat with a fixed nutrient supply and dilution rate. Indeed, the limit $c_0 \ll K$ yields the same steady state as a chemostat (*Appendix D*). Thus, our results for serial dilution include and generalize those obtained for a closely related chemostat model [34]. Critically, it was shown there that in the presence of metabolic trade-offs, the chemostat can support a higher species diversity than prescribed by the competitive exclusion principle. Specifically, if the nutrient supply lies within the convex hull of the strategies on the simplex (visualized by stretching a rubber band around the outermost strategies), an arbitrarily large number of species can coexist at steady state. Note that the coexistence steady state is not single fixed point, but rather a degenerate manifold of possible solutions. Thus, in the chemostat-limit of the cases shown in Figs. 1B and C all the species will coexist. Conversely, if the supply lies outside the convex hull, (e.g., if we swapped the positions of the leftmost species and the supply in Fig. 1B) the number of surviving species would be strictly less than the number

of nutrients, consistent with competitive exclusion. To understand the convex-hull rule, note that a state of arbitrarily high coexistence can only occur if the chemostat self-organizes to a “neutral” state in which the nutrient concentrations are all equal, and thus all strategies have the same growth rate. This state is achieved if and only if the total enzyme abundances lie along the same vector as the nutrient supply, which is achievable only if the supply lies within the convex hull of the strategies present.

Effect of Total Nutrient Bolus on Coexistence

In the chemostat limit, increasing the nutrient supply rate simply proportionally increases the steady-state population abundances. However, away from this limit we find that the magnitude of the nutrient bolus can qualitatively affect the steady-state outcome of serial dilutions. To understand this effect, we first consider a simple case of two nutrients and two species as depicted in Fig. 2A. The two species will coexist if each species is invulnerable to the other. In our example, we first determine the invulnerability of species R (strategy indicated by red circle) by species with strategies lying to its left. To this end, we choose a nutrient supply and perform model serial dilutions until steady state is reached. For a particular finite bolus size, we find that for all supplies within the hatched region an infinitesimal inoculum of any species lying to the left of R will increase more than R during a batch, and therefore can invade R. Similarly, we determine the invulnerability of species B (strategy indicated by blue circle) by any species with a strategy lying to its right, and find the second hatched region. The intersection of these hatched regions for which (1) B can invade R and (2) R can invade B is the supply interval of mutual invulnerability where these two species will stably coexist. The coexistence interval is bounded by the red and blue triangles, and each of these coexistence boundaries is a unique property of its corresponding species. We call these species-specific boundaries *remapped* because they generally lie at different locations on the simplex than the strategies they originated from, with the extent of remapping depending on the nutrient bolus size. (At a more technical level, the remapped boundary for a given species and bolus size is the nutrient supply for which, over the course of a batch, all nutrients are equally valuable).

Since the remapped coexistence boundaries depend on the nutrient bolus size c_0 , changing bolus size can qualitatively change the steady-state outcome of serial dilutions. Figure 2B-D depicts an example of how c_0 affects remapping, and the consequences for species coexistence. At low bolus size, $c_0 \ll K$, corresponding to the chemostat limit, Fig. 2B (left) shows that all species present achieve steady-state coexistence. This follows because the nutrient supply (black diamond) lies inside the convex hull. When c_0 is increased to $c_0 \approx K$ (Fig. 2C), the coexistence boundaries are remapped towards the center of the simplex (dashed arrow). In this example, the nutrient supply now lies outside the convex hull. This results in one winner species (the dark blue one nearest the supply), with all others decreasing exponentially from

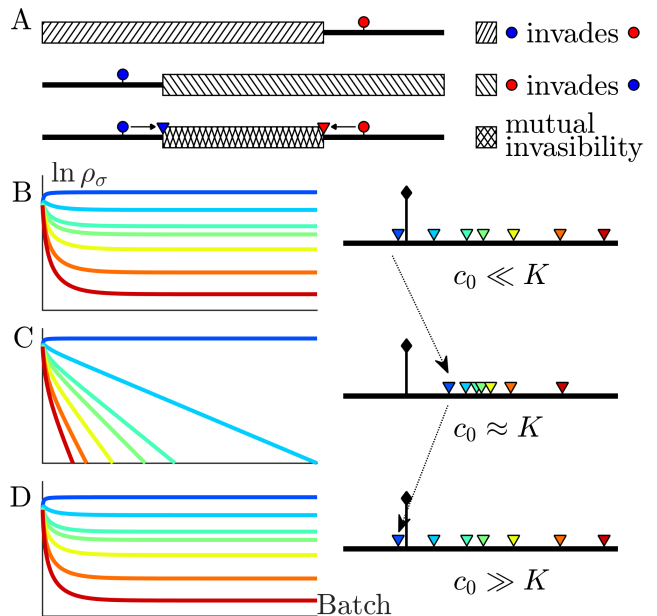


FIG. 2: The nutrient bolus size c_0 affects the relative abundance of species and even their coexistence at steady state. (A) Schematic of the mutual invulnerability condition for two species and two nutrients. Top: The red species can be invaded by any species with a strategy to its left if the supply lies in the region marked by the hatched rectangle. Middle: Similarly, showing the supplies for which blue can be invaded by any species with a strategy to its right. Bottom: The intersection defines a mutual invulnerability region of supplies for which the two species red and blue will coexist. Triangles mark the boundaries of this coexistence region. (B-D) Example of the effect of c_0 on coexistence for more than two species: the approach to steady state, showing $\ln \rho_\sigma$ versus batch number (left column) with the corresponding c_0 -dependent remapping of coexistence boundaries (right column). (B) For the chemostat limit $c_0 \ll K$, where K is the Monod constant for nutrient uptake, the triangles marking coexistence boundaries coincide with the species’ strategies, α_σ . (C) For $c_0 \approx K$ the triangles are remapped towards the center of the simplex compared to the strategies $\{\alpha_\sigma\}$. In this example the nutrient supply (black diamond) ends up outside the coexistence boundaries, so only one species survives. (D) For $c_0 \gg K$ the triangles again coincide with the strategies $\{\alpha_\sigma\}$, leading again to coexistence.

batch to batch. This loss of coexistence with increasing nutrient bolus size is reminiscent of Rosenzweig’s “paradox of enrichment” in predator-prey systems [35]. Strikingly, however, as bolus size is further increased to $c_0 \gg K$, the coexistence boundaries are remapped back to their original positions, so that the nutrient supply once again lies within the convex hull, and so steady-state coexistence of all species is recovered.

Why does the coexistence boundary of a species map back to its original strategy in the limit of large bolus size, $c_0 \gg K$? In this limit, the nutrient uptake functions in Eq. 1 will be saturated during almost the entire period of a batch. Each species will therefore consume nutrients strictly in proportion to its

strategy $\alpha_{\sigma,i}$. For the case of two nutrients (e.g., as shown in Fig. 1B), if there is only a single species present then if the supply lies anywhere to the left of its strategy, at some time during the batch there will be some of Nutrient 2 remaining after the bulk of Nutrient 1 has been consumed. Thus a single species can be invaded by any strategy to its left, provided the supply also lies to its left. Similarly, a species can be invaded by any strategy to its right if the supply lies to its right. This is exactly the condition for the coexistence boundary of a species to coincide with its actual strategy (details in *Appendix E*).

We have rationalized coexistence in our serial dilution model in terms of mutual invasibility, but have not explicitly stated the condition for an arbitrary number of species to coexist in steady state. In the chemostat limit, all species coexist when the concentrations of all nutrients are equal, implying the same growth rate for all strategies. However, for serial dilutions the nutrient concentrations are generally not equal and are not even constant in time. Instead, it is the integrated growth contribution of every nutrient that must be equal to allow for arbitrary coexistence. In the case of equal enzyme budgets ($\varepsilon = 0$), this condition occurs when the time integrals of the nutrient Monod functions within a batch are all equal, i.e.,

$$I_i = \int_0^\infty \frac{c_i}{K_i + c_i} dt = \text{const.} \quad (4)$$

To understand this condition for coexistence beyond competitive exclusion, note that the instantaneous rate of growth of a species σ is $\sum_i \alpha_{\sigma,i} c_i / (K_i + c_i)$, so that the fold increase of a species during a batch is $\exp(\bar{\alpha}_\sigma \cdot \bar{I})$. This fold increase will be equal for all species if and only if Eq. 4 holds. When there are two nutrients, Eq. 4 holds at steady state whenever the supply is inside the convex hull of the coexistence boundaries of the species present (details in *Appendix C*). For more nutrients, the corresponding condition is that the region of coexistence is bounded by contours that connect the outermost remapped nodes.

Steady-state Diversity

As is apparent in Fig. 2C, not all strategies are remapped to the same extent. In Fig. 3A, we plot the remapping of coexistence boundaries as a function of nutrient bolus c_0 . Note that: (i) the specialists (0, 1) and (1, 0) and the perfect generalist (0.5, 0.5) are not remapped at all; (ii) remapping is maximal for $c_0 \approx K$; (iii) there is no remapping in both the $c_0 \rightarrow 0$ and $c_0 \rightarrow \infty$ limits (see also *Appendix Fig. 9*). The extent of remapping also depends on the inoculum size ρ_0 as shown in Fig. 3B, which demonstrates that remapping is maximal for $\rho_0 \ll K$ and vanishes for $\rho_0 \gg K$.

How does remapping influence steady-state species diversity? A useful summary statistic for quantifying diversity [36] is the effective number of species $m_e = \exp[-\sum_\sigma P_\sigma \ln P_\sigma]$ where $P_\sigma = \rho_\sigma(0)/\rho_0$. Diversity as measured by m_e is shown in Fig. 3C for six choices of nutrient bolus composition. Notably, if the two nutrients are supplied equally (top curve,

magenta), m_e is independent of c_0 and coincides with the maximal possible diversity (dashed black line), namely equal steady-state abundances of all species (Fig. 3D, top). Conversely, if Nutrient 1 comprises only 5% of supplied nutrient (Fig. 3C, bottom curve, cyan), the number of effective species m_e is lower than maximal even in the chemostat-limit of small bolus sizes $c_0 \ll K$ and drops even further for $c_0 \approx K$. This loss of diversity is due to the dramatically lowered steady-state abundances of strategies that favor Nutrient 1 (Fig. 3D, bottom). For very large bolus sizes, diversity returns to its chemostat-limit, as expected from the lack of remapping for $c_0 \gg K$. Though here we focused on the case of two nutrients, these results extend to more nutrients (for three nutrients see *Appendix Fig. 18*).

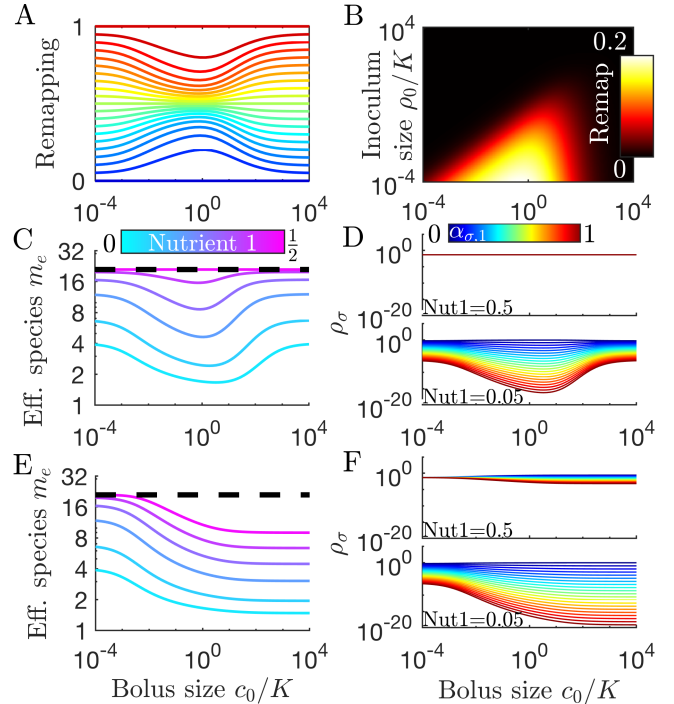


FIG. 3: Remapping of strategies at finite nutrient supply generally reduces species diversity. (A) As shown for the case of two nutrients, the remapping of strategies (i.e., the shift of coexistence boundaries) is non-monotonic with nutrient bolus size c_0 (colors indicate 21 equally spaced strategies). (B) Heat map of the extent of remapping for strategy (0.2, 0.8) as a function of nutrient bolus size c_0/K and inoculum size ρ_0/K . (C) Steady-state effective number of species m_e as a function of bolus size c_0/K with equal initial inocula adding up to $\rho_0/K = 10^{-3}$; the same initial conditions apply for panels D-F. Colors correspond to different nutrient supply compositions $c_1/(c_1 + c_2)$. Dashed black line: maximum diversity (equal species abundances) is attained when nutrient composition is (0.5, 0.5). (D) Steady-state species abundances $\{\rho_\sigma\}$ for nutrient composition (0.5, 0.5) (top) and (0.05, 0.95) (bottom). (E, F) Same as C, D but with two trophic layers with Nutrient 1 a byproduct of metabolizing Nutrient 2: (E) effective number of species m_e and (F) species abundances ρ_σ .

Cross-feeding

It is possible to extend Eqs. 2 and 3 beyond a single trophic layer, allowing for consumption of metabolic byproducts. This is a form of cross-feeding, which has generally been found to promote diversity [10] and stable community structure [19]. Here, cross-feeding is introduced through the byproduct matrix $\Gamma_{i,i'}^\sigma$, which converts the consumption of nutrient i' to production of nutrient i such that,

$$\frac{dc_i}{dt} = - \sum_{\sigma} \rho_{\sigma} \left(j_{\sigma,i} - \sum_{i'} \Gamma_{i,i'}^{\sigma} j_{\sigma,i'} \right). \quad (5)$$

We focus on the simplest case: initially supplying only Nutrient 2, with Nutrient 1 solely derived as a metabolic byproduct via $\Gamma_{i,i'}^\sigma = \begin{pmatrix} 0 & \Gamma \\ 0 & 0 \end{pmatrix}$ for all species. When $\Gamma = 1$, upon consumption Nutrient 2 is perfectly converted to Nutrient 1, leading to an equal total supply of the two nutrients. More generally, $\int_0^\infty \sum_{\sigma} \rho_{\sigma} j_{\sigma,1} dt = \Gamma c_2(0)$ which allows a direct comparison between the unitrophic and bitrophic regimes: starting with $c_2(0)$ nutrient results in $(\Gamma + 1)c_2(0)$ total nutrient, and hence the Nutrient 1 fraction is $\frac{\Gamma}{1+\Gamma}$ of the total.

How does cross-feeding influence diversity in our serial dilution model? In Fig. 3E we compare bitrophic diversity for six values of Γ to their unitrophic equivalents (in Fig. 3C). We note that: (i) bitrophy still supports diversity greater than the competitive-exclusion limit; (ii) in the chemostat regime, $c_0 \ll K$, the unitrophic and bitrophic schemes have identical values of m_e , and these drop as $c_0 \rightarrow K$; (iii) but for bitrophy the m_e does not recover for $c_0 \gg K$; (iv) even when the total supply of both nutrients is equal ($\Gamma = 1$), bitrophy leads to lower than maximal m_e outside the chemostat limit. These features are clarified in Fig. 3F, which shows steady-state species abundances for Γ values leading to a total Nutrient 1 supply fraction of 0.5 and 0.05, and highlights the lower diversity for bitrophy compared to unitrophy for large nutrient bolus size. This difference is due to an "early-bird" effect: a species consuming supplied nutrient early in the batch can build a sizable population before the competing species that rely on its byproduct. The early-bird population then outcompetes the others for byproduct consumption. As such, this effect increases with c_0/ρ_0 ; the effect also becomes stronger at low c_0/K , since this allows the early-bird species more time to grow more before the byproduct accumulates to high enough levels to be significantly consumed (Appendix Fig. 10).

Population Bottlenecks

So far we have considered deterministic dynamics, which is appropriate for large populations. In natural settings, however, there are often small semi-isolated communities. For these communities, fluctuations can play an important role. In particular, population bottlenecks can lead to large demographic changes [37]. How does the nutrient supply affect

diversity in such communities? To address this question, we applied discrete sampling of a finite population when diluting from one batch to the next (see Appendix A). With this protocol, an "extinction" occurs when sampling yields zero individuals of a species. For a long enough series of dilutions such extinctions would ultimately lead to near-complete loss of diversity. For small real-world populations, however, diversity may be maintained by migration. To model such migration we augmented the population at each dilution with a "spike-in" from a global pool of species, in the spirit of MacArthur's theory of island biogeography [38].

In Fig. 4A we show results of spike-in serial dilutions for a population bottleneck of 1000 cells. 95% of these cells are sampled from the previous batch, while 5% are sampled from a global pool, with equal abundances of 21 equally spaced strategies (*cf.* Fig. 3A). The resulting m_e vs. c_0 curves have maximal m_e for all six nutrient fractions in the regime $c_0 \ll K$ where the 5% spike-in dominates sampling noise. As expected, for a balanced nutrient supply at any c_0 , all species have the same average abundance (Fig. 4B top). By contrast, when Nutrient 1's fraction is low (Fig. 4A cyan and 4B bottom), increasing c_0 increases the abundance gaps between the species, reflecting the uneven competition for Nutrient 2. Overall, the spike-in protocol leads to higher diversity at low c_0 than the deterministic case (starting from equal species abundances but with no spike-in, Fig. 3C). For large c_0 , the m_e vs. c_0 curves for these two protocols are indistinguishable. The only noticeable difference is that the spike-in maintains a higher level of the least competitive strains, but since these abundances are still low, this difference is not reflected in the m_e values.

Unequal enzyme budgets

While we have assumed exact trade-offs to achieve diversity within a resource-competition model, the trade-offs present among real microorganisms will not be exact. For the serial dilution protocol with spike-ins, diversity is maintained by migration and so it is possible to relax the constraint of exact trade-offs. How does diversity depend on the nutrient supply if we allow species to have different enzyme budgets? We implemented random differences in species enzyme budgets by setting $\varepsilon = 0.1$, i.e. a standard deviation of 10%, and plotted effective number of species m_e in Fig. 4C. As in the $\varepsilon = 0$ limit (Fig. 4A), at sufficiently small c_0 the spike-in procedure dominates both sampling noise and differential growth rates due to unequal enzyme budgets. Raising c_0 leads to a drop in m_e (albeit still above the competitive-exclusion limit). Examining the species abundances in Fig. 4D, we note that differences in enzyme budget establish a fitness hierarchy even when nutrient fractions are equal (top), with those species with the highest budgets increasing in relative abundance as c_0 increases. The asterisk (*) marks the species with the highest total enzyme budget, which becomes the most abundant for $c_0 > K$. Reducing Nutrient 1's fraction to 0.05 results in a shifting abundance hierarchy (Fig. 4D, bottom): at low c_0 the highest abundance species is the one that consumes

only Nutrient 2, as in the equivalent $\varepsilon = 0$ case. However, increasing c_0 results in increased abundance for the species with the highest enzyme budget – which would ultimately lead to its domination for sufficiently large c_0 . In short, for spike-in serial dilutions the influence of unequal enzyme budgets depends on the nutrient supply, such that the species with the largest budgets dominate for large, unbiased supplies.

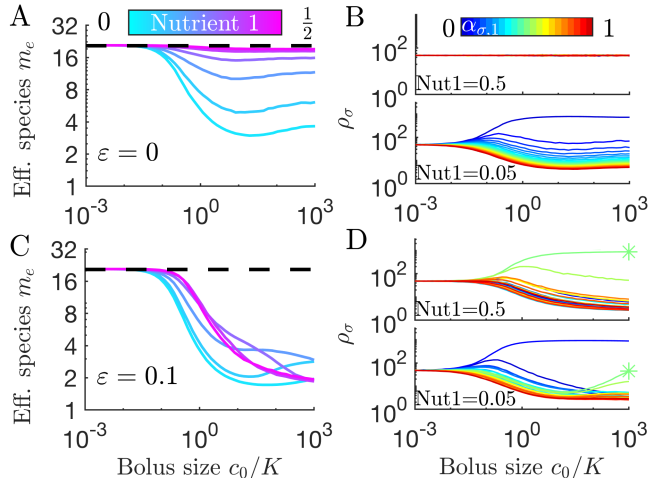


FIG. 4: Diversity of small communities with migration. Each batch was inoculated with 1000 cells: 950 cells sampled without replacement from the previous batch, 50 cells sampled from 21 equally abundant, equally spaced strategies. (A) Effective number of species m_e for different compositions of two nutrients (colors) as a function of nutrient bolus size c_0/K . (B) Average steady-state species abundances $\{\rho_\sigma\}$ for nutrient composition (0.5, 0.5) (top) and (0.05, 0.95) (bottom). (C) as A, but with random species-specific total enzyme budget specified by $\varepsilon = 0.1$. (D) as B but with species-specific enzyme budgets from C. Asterisk (*) indicates the species with the largest enzyme budget.

Mutation-Selection Balance

So far, we have considered experimental serial dilution systems as a proxy for the variable nutrient supply of natural ecosystems. To more closely capture the dynamic equilibrium of populations in the wild, we extend our model to include mutation-selection balance. Specifically, we introduce mutations as random changes in metabolic strategy [39]. Since a mutant is initially present as a single cell, it becomes essential to stochastically model the population dynamics, including both reproduction and sampling for each inoculum. Within a batch, instead of the deterministic ODEs of Eqs. 2-3 we simulate stochastic dynamics using Gillespie’s method, summarized in Table I in Appendix A. For large populations, the resulting steady state matches the deterministic one, including the remapping observed in Fig. 3A (see Appendix Fig. 11). To account for mutations, we modify the growth term to allow for *mutation*, whereby when species σ grows by one cell, instead

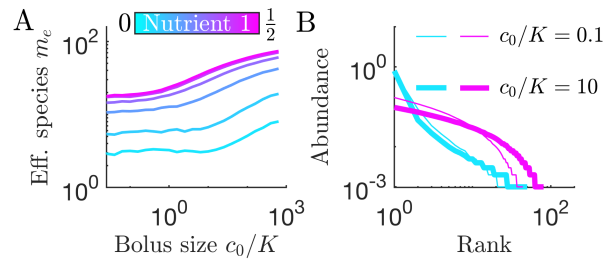


FIG. 5: Diversity of species under mutation-selection balance. Starting from an inoculum of 1000 cells, a fraction $\nu = 0.01$ of cell divisions results in a mutation to a randomly-selected one of 201 evenly spaced strategies. Populations recorded at the start of each batch. (A) Effective number of species m_e for different nutrient compositions (colors) as a function of nutrient bolus size c_0/K . (B) Rank-abundance curves for Nutrient 1 fractions 0.05 (cyan) and 0.5 (magenta); line thickness indicates value of c_0/K .

of making another σ , it makes a σ' cell, i.e. $\sigma \rightarrow \sigma + \sigma'$. *Mutation* occurs at a rate $\nu\rho_\sigma \sum_i j_{\sigma,i}$, while normal growth, $\sigma \rightarrow 2\sigma$, occurs at a rate $(1-\nu)\rho_\sigma \sum_i j_{\sigma,i}$. Together, stochastic reproduction, inter-batch sampling, and intra-batch mutations lead to complex dynamics whereby a species can appear, flourish for a number of batches, then die out, with different species replacing it. This results in fluctuations in the number of species present from batch to batch (Appendix Fig. 12 and Fig. 13).

How does species diversity depend on nutrient bolus size c_0 under conditions of mutation-selection balance? Previously, we saw that diversity decreased for $c_0 \approx K$ due to the remapping of coexistence boundaries. Now with mutations, the larger the nutrient bolus c_0 , the more mutations within a batch, leading to more species at the end of the batch (Appendix Fig. 14). How do these opposing tendencies combine? Figure 5A shows the effective number of species, m_e . As c_0 increases, the decrease in m_e due to remapping is offset by mutations generating new species. As a result, for these parameters, m_e is flat as $c_0 \approx K$. As c_0 increases further, m_e does increase, due to both mutations and reduced remapping. This is evident in Fig. 5B which shows more species and flatter rank-abundance curves for higher c_0 for a balanced nutrient supply (magenta). Even for an unbalanced nutrient supply (cyan), diversity increases for large enough c_0/K . (Lower values of c_0/K are shown in Appendix Figs. 15, 16). Broadly speaking, mutations in our model lead to a “rich get poorer” effect in which high-abundance species feed low-abundance species with a steady stream of mutants, leading to higher overall species diversity.

Comparison of model framework with experimental data

We have explored the implications of our model in a variety of contexts, but how well does our framework of substitutable and simultaneous consumption of nutrients reflect how microbes grow in nature? In artificial media with high nutrient

levels (e.g. \sim g/L of sugar), a pattern of sequential utilization is often observed where a preferred nutrient (often glucose) is consumed before others [40]. However, these artificially high nutrient levels are far above the nutrient levels typically found in natural environments [41]. At these lower concentrations, simultaneous utilization of multiple substitutable nutrients is often observed [33, 42, 43]. We therefore compared our modeling framework to previously published data from chemostat and batch experiments on *E. coli* supplied with multiple sugars at low concentrations.

We use chemostat data from Lendenmann et al. [43] who measured the steady-state concentrations of biomass and sugars, with *E. coli* continuously supplied with mixtures of glucose, fructose, and ribose. We applied the chemostat version of the model [34] and constrained the fit with previously measured values of the Monod constants K_i for this strain [44]. From the fit, we estimated the consumption strategies α_i for glucose, fructose, and ribose, with the rest of the parameters being defined experimentally (see Appendix A for values of these parameters). As shown in Figs. 6A and B, the resulting model matches the data well with strategies, measured in $(\text{mg sugar})(\text{mg biomass})^{-1}\text{h}^{-1}$, of $\alpha_{\text{gluc}} = 1.96 \pm 0.12$, $\alpha_{\text{fruc}} = 2.04 \pm 0.11$, and $\alpha_{\text{ribo}} = 1.41 \pm 0.01$. This corresponds to a normalized strategy of (0.36, 0.38, 0.26). The only notable deviations between the best-fit model and the data occurs for two fructose steady states. These deviations would be corrected if K_{fruc} was larger, suggesting that the K_{fruc} used here may not reflect the actual value in the experiment. The model also accurately predicts the resulting steady-state biomass concentrations, which are a constant 47 mg/L in the experiment and approximately constant at 45 mg/L in our model. As a whole, the overall good agreement suggests that our model assumptions are consistent with the behavior of *E. coli* growing at low nutrient concentration with a continuous nutrient supply. Despite being supplied with a variety of different sugar mixtures, *E. coli* maintains a constant steady-state biomass in these experiments because all of the carbon sources are substitutable.

To explicitly test growth dynamics, we compared our model to batch growth data from Egli et al. [42]. In this experiment, timecourses of biomass and nutrient concentrations were measured in a culture of *E. coli* supplied with a mixture of glucose and galactose. The *E. coli* used to seed this culture came from a glucose-limited chemostat (we also compared our model to a batch seeded with *E. coli* from a galactose-limited chemostat, see Appendix Fig. 17). For this data we used our serial dilution model with Monod kinetics and K_i values from measurements on the same strain [44]. As shown in Fig. 6C, the agreement between the best-fit model and the experimental data is generally quite good over the entire time course. The estimated α_i , measured in units of $(\text{mg sugar})(\text{mg biomass})^{-1}\text{h}^{-1}$, were 0.46 ± 0.04 and 0.41 ± 0.03 for glucose and galactose, respectively. The estimated yield was $0.42 \pm 0.03 (\text{mg biomass})(\text{mg sugar})^{-1}$, similar to the experimentally measured yield used in the chemostat model of $0.45 (\text{mg biomass})(\text{mg sugar})^{-1}$. Our model captures the glucose and biomass trends very well, but some galactose data points fall outside of the confidence interval.

In addition to possible experimental noise, this may be due to small variations in yield during growth, as a constant yield would imply that accurately modeling biomass and glucose would necessarily also accurately capture galactose ($c_{\text{gal}}(t) = \text{const} - \rho(t) - Y c_{\text{gluc}}(t)$). A time-varying yield would explain why the system appears to slightly increase in total effective biomass during the middle of the timecourse. Nevertheless, it is clear that the overall growth dynamics in this experiment are consistent with our model assumptions, including substitutable and simultaneous consumption of nutrients.

While we only compare our model to data from *E. coli*, substitutable and simultaneous growth on multiple nutrients has been observed in other bacteria such as *Lactobacillus brevis* [45], and has even been observed in non-prokaryotic organisms. For example, the eukaryote *Kloeckera sp. 2201* has been shown to simultaneously utilize methanol and glucose as carbon sources [33]. Similarly, the methanogenic archaeon *Methanosarcina barkeri* can simultaneously utilize methanol and acetate in batch culture [46]. However, it should be noted that our simple model framework cannot describe the growth kinetics of all microbes in all conditions. For example, the inferred strategy of *E. coli* for glucose varied between the batch and chemostat experiments examined here, suggesting that the total metabolic enzyme budget of microbes changes in different conditions. Such variation is likely due to other cell functions, such as ribosome synthesis [47], consuming different fractions of the cell's total material and energy budget, something we do not explicitly model. Indeed, our goal is not to precisely model all microbial growth phenomenon, but rather to construct a widely applicable approximation of microbial growth in order to better understand ecological dynamics.

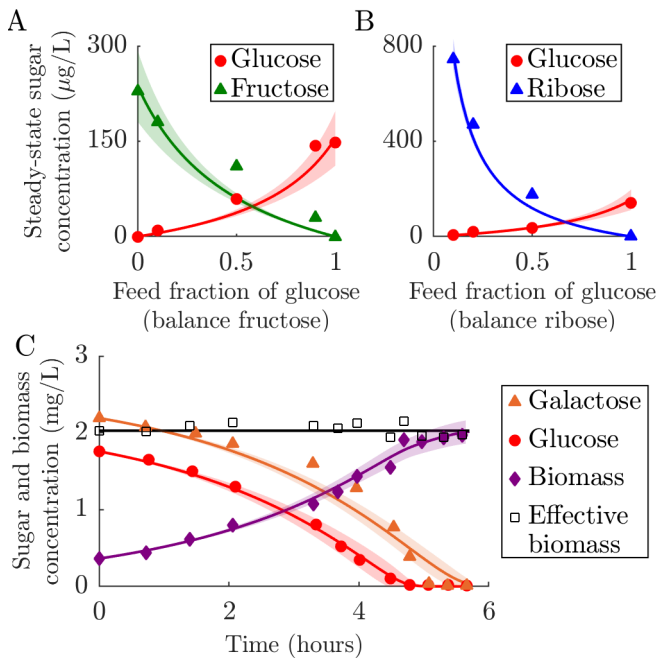


FIG. 6: Fitting of fixed-enzyme-budget model to experimental data. (A-B) Fit of the chemostat version of the model to data from chemostat experiments from Lendenmann et al. [43]. The experimental data are steady-state concentrations of sugars in *E. coli* chemostats supplied with different mixtures of glucose, fructose, and ribose. The strategy α_i for each sugar is inferred, whereas all other parameters are derived from the experimental conditions and measurements. The solid curves show the model prediction, with the shaded region marking the 95% prediction bound (see Appendix A for details). (A) Comparison of model to data from chemostats supplied with glucose and fructose with a constant total feed concentration of 100 mg/L. (B) Comparison of model to data from chemostats supplied with glucose and ribose with a constant total feed concentration of 100 mg/L. (C) Comparison of serial dilution model fit to batch growth data from Egli et al. [42]. Solid curves are model predictions and the shaded area is the 95% prediction bound. “Effective biomass” refers to the total biomass within the system: $M(t) = \rho(t) + Y(c_{\text{gluc}}(t) + c_{\text{gal}}(t))$. Since the data for the three timeseries were measured at slightly different times, the effective biomass for the experimental data was obtained by linear interpolation of the data points. The inferred parameters were the strategy (α_1, α_2) for the two sugars, glucose and galactose, and the yield Y .

Discussion

Natural ecosystems experience variations in the timing and magnitude of nutrient supply, and the impact of these variations on species diversity is not fully understood [22, 32]. To explore the impact of variable nutrient supply, we modeled resource competition in a serial dilution framework and analyzed the model’s steady states. We found that variable nutrient supply still allows for the high diversity seen in the

continuous supply (“chemostat”) version of the model. Surprisingly, however, supplying the nutrients as a bolus led to a dependence of diversity on the amount of supplied nutrients.

Finding a general relation between the amount of nutrient supplied to a community and its diversity is a long-standing goal of theoretical ecology [23–25]. We found that in our model the form of the nutrient-diversity relation (NDR) can change based on model details. The model has two regimes: a low diversity and a high diversity regime. The former satisfies competitive exclusion (no more species coexisting than resources), whereas the latter exceeds competitive exclusion and occurs when the nutrient supply lies within the convex hull of the remapped metabolic strategies present [34]. At the bifurcation point between the two regimes, we observe critical slowing down in that the number of dilutions required to reach steady state diverges. An interesting direction for future research will be to characterize this divergence and the resulting interplay between relaxation to steady state and response to slowly changing environmental conditions.

In the high diversity regime, the NDR can take several forms. For a single trophic layer and multiple supplied nutrients, the model has a U-shaped NDR. For a single supplied nutrient with cross-feeding via a second trophic layer, the NDR is monotonically decreasing. Finally, allowing daughter cells to have different strategies than their parents (“mutation”) leads to a monotonically increasing NDR. Thus, even in this very simple model there is no general NDR.

Experimental studies that characterize the NDRs of microbial ecosystems have reached similarly variable conclusions. For example, one work studying bacterial communities in Arctic deep-sea sediments found an increasing trend between energy input and richness [29], while a study on photosynthetic microbial mats found a negative relationship between energy input and richness [30]. A meta-analysis of aquatic microbial ecosystems found examples of both monotonic and non-monotonic NDRs, with no single form dominating [32]. Our theoretical results, together with these experimental findings, indicate that there may be no single universal NDR in microbial ecosystems. This conclusion suggests that the best approach for characterizing the NDR of a given ecosystem is not to apply a one-size-fits-all theory, but to analyze the role of different factors such as cross-feeding, trade-offs, and immigration in determining that particular ecosystem’s NDR. While we have focused on microbial systems, the absence of a universal NDR is consistent with results from recent work in plants [28].

We found that the stringency of metabolic trade-offs has a large impact on community diversity. We imposed a metabolic enzyme budget on each species to reflect the reality that microbial cells have a finite capacity to synthesize proteins and must carefully apportion their proteome [48]. However, while it is true that microbes have limited biosynthetic capacity, it is unclear how strict are the resulting trade-offs. For this reason, we characterized versions of the model with both exact and inexact trade-offs. Our results show that the form of an ecosystem’s NDR can depend on the stringency of metabolic trade-offs. This finding is not exclusive to the serial dilution model. The stringency of trade-offs was also

important in the original chemostat setting: in a birth-death-immigration framework, small violations of the enzyme budget still allowed for high levels of coexistence, but large violations disrupted coexistence [34]. These results suggest that an experimental characterization of the stringency of metabolic trade-offs among microbes would provide a valuable ecological parameter. Also note that metabolic trade-offs are only one of the many types of trade-offs microbes are subject to; other types of trade-offs, such as constraints between biomass yield and growth rate [49], may also shape a community’s NDR.

In constructing a model, we made a number of assumptions about the way in which microbes consume and utilize nutrients. Some of these assumptions do not apply to all microbial communities, and it would be worthwhile to examine the impact of relaxing these assumptions on the NDR. For example, we focused on communities where all nutrients are equally valuable (i.e. $Y_i = Y_j \forall i, j$). However, biomass yields can vary between nutrients and between species. We show in Fig. 8 that coexistence in the serial dilution model is robust to varying yield, as long as all species have the same yield on a given nutrient. The scenario where species have different biomass yields on the same nutrient is conceptually similar to the case of inexact trade-offs, since some species will have a strict advantage over others. Thus, it is likely that these unequal yields between species will lead to a reduction in community diversity. However, varying the yield in this manner also allows for the inclusion of new trade-offs that may impact diversity, such as the aforementioned trade-off between yield and growth rate [49]. Our model framework also assumes that all nutrients are substitutable (i.e. only one of the multiple nutrients is required for growth). In real ecosystems, microbes can require multiple complementary nutrients to grow, e.g. sources of carbon, nitrogen, and phosphorus. In cases where one class of complementary nutrient is strongly limiting, a model with both complementary and substitutable resources would essentially reduce to the current model of only substitutable resources. This case is likely the more common one, e.g. as many soils are carbon limited [50, 51]. However, in cases where no single nutrient is strongly limiting, the presence of complementary nutrients would possibly lead to different NDRs, which will be an interesting direction for future study. Another potentially informative alteration to our model is to relax the assumption of constant enzyme levels by adding metabolic enzyme regulation in response to nutrient levels. This would allow species’ strategies to move through the simplex as a batch progresses. Since the position of the strategies controls the remapped node positions, the addition of enzyme regulation could impact community diversity and coexistence.

Our modeling predictions, e.g. the convex hull condition and the high diversity resulting from “spike-in” even when enzyme budgets are unequal, are in principle testable. As we showed in Fig. 6, the growth dynamics of *E. coli* at low nutrient levels is well described by our modeling framework. The experiments we compared to were performed with the same strain of *E. coli*, meaning different microbes would be needed to test the multispecies predictions. To determine the strategies of other microbes, including other strains of *E. coli*, the most practical approach would likely be batch culturing. Once

strains with different strategies have been identified, nutrient-diversity relationships could then be obtained by competing strains in serial dilution culture and measuring the community diversity (e.g. via fluorescent tags or by 16S rRNA sequencing) as a function of the total concentration of sugars provided at the start of each batch.

Acknowledgments

This work was supported by National Institutes of Health (www.nih.gov) Grant R01 GM082938 (A.E., Y.M., and N.S.W.), and National Science Foundation Grant GRFP DGE-1656466 (J.G.L.). N.S.W. supervised the research; A.E. and J.G.L. wrote simulations and did analytic calculations; all authors interpreted results; A.E., J.G.L., and N.S.W. wrote the paper. All code and data used in this manuscript available at <https://github.com/AmirErez/SeasonalEcosystem>.

Appendix A: Methods

This section describes the simulation methods used in this manuscript. All code and data used in this manuscript can be found at <https://github.com/AmirErez/SeasonalEcosystem>.

Deterministic dynamics

We numerically solve the ODEs within each batch using a custom MATLAB-coded fourth-order Runge-Kutta solver with adaptive step size. Step size at a given time step is chosen such that the relative change of all state variables is below a predetermined threshold.

Population bottleneck sampling

We implement discrete sampling when diluting from one batch to the next by picking without replacement ρ_0 individuals from a total end-of-batch population of $\rho_0 + c_0$. If there are non-integer populations at the end of a batch (as can occur with deterministic dynamics), they are rounded up if $\rho_\sigma - \text{floor}(\rho_\sigma) > U(0, 1)$ where floor rounds down to the nearest integer and $U(0, 1)$ is a uniform random variable between 0 and 1. For all simulations with stochastic bottlenecks, we allow the simulation to equilibrate for 10,000 dilutions and average over 10,000 further dilutions.

Mutation-selection dynamics

We use Gillespie’s algorithm to simulate the reactions shown in Table I until all nutrients $\{c_i\}$ are depleted.

TABLE I: Gillespie reactions for mutation-selection dynamics

Name	Reaction	Rate
Birth	$\sigma \rightarrow 2\sigma$	$(1 - \nu)\rho_\sigma \sum_i j_{\sigma,i}$
Mutation	$\sigma \rightarrow \sigma + \sigma'$	$\nu\rho_\sigma \sum_i j_{\sigma,i}$ for a randomly chosen σ'
Time	$t \rightarrow t + \Delta t$	$\Delta t = -\ln(U(0,1))/\sum_{\sigma,i} \rho_\sigma j_{\sigma,i}$

with $U(0,1)$ a uniform random variable between 0 and 1. For each ‘‘birth’’ reaction, $(\rho_\sigma$ increases by 1), c_i decreases by $j_{\sigma,i}/\sum_i j_{\sigma,i}$.

For all simulations featuring mutation (Fig. 5 and Appendix Figs. 12-16), we let the system equilibrate over 10,000 dilutions, much more than required to reach steady state in the deterministic model, and then average over at least 90,000 more dilutions. To ensure that the results do not depend on the number of possible strategies, (due to mutations saturating all possible species), we increase the total number to 201 species equally spaced between 0 and 1.

TABLE II: Annotation glossary

Symbol	Description
t	Time measured from the beginning of a batch
p	Number of nutrients
m	Number of species introduced at time $t = 0$
m_e	Effective number of species at steady state
ν	Mutation rate
i	$(1..p)$ Latin index enumerating nutrients
$c_i(t)$	Time dependent concentration of nutrient i
c_0	$\sum_{i=1}^p c_i(0)$; total nutrient concentration at time $t = 0$
$K_i \equiv K$	Monod half-velocity constant
I_i	$\int_0^\infty \frac{c_i}{K_i + c_i} dt$; nutrient Monod function time integral
σ, σ', \dots	$(1..m)$ Greek indices enumerating species
$\rho_\sigma(t)$	Species σ biomass density at time t since a start of the batch
$\tilde{\alpha}_\sigma$	$(\alpha_{\sigma,1}, \dots, \alpha_{\sigma,p})$; enzyme allocation strategy for species σ
ε	Standard deviation in enzyme budget
E	$E = \sum_i \alpha_{\sigma,i} = 1$ for $\varepsilon = 0$; enzyme budget
$\Gamma_{i,i'}$	Byproduct matrix converting nutrient i' to nutrient i
$j_{\sigma,i}$	Nutrient i consumption rate by species σ
Y_i	Biomass yield on nutrient i

Fitting to experimental data

To fit our model to the experimental data in Lendenmann et al. [43], we first digitally extracted the steady-state data points from the experimental figures. We used the model from Posfai et al. [34] with Monod kinetics. The K_i of glucose, ribose, and fructose were taken as 73, 132, and 125 $\mu\text{g/L}$ sugar, respectively [44]. The model was fit to the data and the standard error of parameters were estimated using the MATLAB curve fitting toolbox. The only parameters estimated were the α_i of glucose, ribose, and fructose. It was assumed that all sugars had a biomass yield of $Y = 0.45$ (g biomass)(g sugar) $^{-1}$, as

measured experimentally [43]. The supply rates for a given simulation were computed as $S_i = c_{f,i}\delta$, where S_i is the nutrient supply rate of nutrient i , $c_{f,i}$ is the concentration in the feed of nutrient i , and δ is the dilution rate of the chemostat. The fitting process minimized only the sum of squared errors between the model and the nutrient concentration data, since steady-state biomass within the model is approximately constant and determined by measured parameters ($\rho_{ss} \approx \frac{Y \sum_i S_i}{\delta}$). Confidence intervals for parameters were estimated using MATLAB’s *confint* function, which computes the interval using an estimate of the diagonal elements of the covariance matrix of the coefficients multiplied by the inverse of the Student’s t distribution. The prediction bounds (shaded regions) are calculated using MATLAB’s *predint* function, which uses the estimated covariance matrix and the Jacobian of the fitted values to the parameters to predict the bounds.

The data fitting procedure for the batch experimental data was similar to that employed for the chemostat experimental data. We digitally extracted the data points from the figure in Egli et al. [42] and used the MATLAB curve fitting toolbox. The biomass was reported as OD_{546} and was converted to mg/L using a conversion factor measured for the same strain [43]. Two sugar data points that were taken before the first biomass measurement were removed so that the initial conditions of the system would be well-defined. We estimated the parameters of the serial dilution model developed in this paper assuming Monod kinetics (Eq. 1). It was further assumed that both sugars had the same yield, Y . The yield was not measured in the experimental study and was therefore left as a fitting parameter. The K_i for glucose and galactose were 73 and 98 $\mu\text{g/L}$, respectively [44]. The three fitting parameters were the yield Y and the strategies α_i for glucose and galactose. The data points of the sugar and biomass measurements were taken at slightly different times, so the effective biomass for the experimental data was obtained by linear interpolation of the data points. Confidence intervals and prediction bounds were estimated using the same methods as for the chemostat model.

Appendix B: General form of the model

The most general form of the model considered in this manuscript includes variable nutrient yield Y_i , Monod half-velocity constant \tilde{K}_i , and enzyme cost w_i :

$$\frac{d\rho_\sigma}{dt} = \sum_i \tilde{Y}_i \tilde{\alpha}_{\sigma i} \rho_\sigma \frac{\tilde{c}_i}{\tilde{K}_i + \tilde{c}_i} \quad (\text{B1})$$

$$\frac{d\tilde{c}_i}{dt} = - \sum_\sigma \tilde{\alpha}_{\sigma i} \rho_\sigma \frac{\tilde{c}_i}{\tilde{K}_i + \tilde{c}_i} \quad (\text{B2})$$

$$E = \sum_i w_i \tilde{\alpha}_{\sigma i}. \quad (\text{B3})$$

The enzyme costs w_i and total enzyme budget E of the original equations can be removed by rescaling the strategies and nutrient concentrations such that $\tilde{\alpha}_{\sigma i} = (E/w_i)\alpha_{\sigma i}$ and $\tilde{c}_i = (E/w_i)c_i$. This rescaling leads to a new effective Monod

half-velocity constant and yield such that $\tilde{K}_i = (E/w_i)K_i$ and $\tilde{Y}_i = (w_i/E)Y_i$. The simplified equations are therefore:

$$\frac{d\rho_\sigma}{dt} = \sum_i Y_i \alpha_{\sigma i} \rho_\sigma \frac{c_i}{K_i + c_i} \quad (\text{B4})$$

$$\frac{dc_i}{dt} = - \sum_\sigma \alpha_{\sigma i} \rho_\sigma \frac{c_i}{K_i + c_i} \quad (\text{B5})$$

$$1 = \sum_i \alpha_{\sigma i}. \quad (\text{B6})$$

Appendix C: Mutual invasibility condition for coexistence beyond competitive exclusion

In our model, coexistence of an unlimited number of species can be traced back to the conditions for the coexistence of a smaller number of species. This is because in a system with p nutrients, once p species coexist they create an environment where all nutrients are equally valuable and all species can coexist. For example, understanding the conditions for unlimited coexistence in two nutrient competition requires us to examine the conditions that allow two species to coexist. In order for two species to coexist, they must be able to invade each other. This means that in an environment dominated by Species 1, Species 2 will have higher fitness and vice-versa.

Under what nutrient supplies, $c_i(0)/c_0$, can two species invade each other? In the chemostat version of the model, these invasibility conditions are simple to determine. Consider two species where $\bar{\alpha}_1$ is to the left of $\bar{\alpha}_2$ on the 1-simplex. Species 2 can invade Species 1 if the nutrient supply is to the right of $\bar{\alpha}_1$. Species 1 can invade Species 2 if the nutrient supply is to the left of $\bar{\alpha}_2$. Therefore, the two species can mutually invade and coexist if and only if the nutrient supply lies between $\bar{\alpha}_1$ and $\bar{\alpha}_2$. This is precisely the convex hull condition, with no remapping.

For same pair of species, how do we determine the nutrient supplies for which species 1 can be invaded by Species 2 in the serial dilution version of the model? The fitness of a species in this model is the growth exponent $\sum_i \alpha_{\sigma i} I_i$, meaning that species 2 can invade Species 1 at nutrient supplies where Species 1 creates an environment such that $I_2 > I_1$. The nutrient supply at which Species 1 creates an environment where $I_1 = I_2$ therefore bounds the region of nutrient supplies for which Species 2 can invade. By the same logic, the border for the region where Species 1 can invade Species 2 is the nutrient supply at which Species 2 creates an environment where $I_1 = I_2$. Therefore, the mutual invasibility region is now defined by the nutrient supplies where each species growing in isolation creates an environment where $I_1 = I_2$. These points are what we refer to as the "remapped coexistence boundaries" and, unlike in the chemostat version of the model, these generally do not correspond to the species' strategies.

Appendix D: Perturbation theory for $c_0/K_i \ll 1$

In the main text, we provide an explanation why in the limit of small nutrient bolus size c_0/K , the serial dilution model becomes a chemostat. In this section, we prove this chemostat limit using a perturbation expansion to first order in c_0/K .

We define a perturbation expansion with respect to the small parameter $\phi = c_0/K$,

$$\begin{aligned} \rho_\sigma(t) &= \rho_\sigma(0) + \phi \rho_\sigma^{(1)}(t) + \phi^2 \rho_\sigma^{(2)}(t) + \dots \quad (\text{D1}) \\ c_i(t) &= \phi c_i^{(1)}(t) + \phi^2 c_i^{(2)}(t) + \dots \\ \rho_\sigma^{(k>0)}(0) &= 0 \\ c_i^{(k>1)}(0) &= 0. \end{aligned}$$

We note that at $O(1)$ we have $\rho_\sigma(t) = \rho_\sigma(0)$ and $c_i(t) = 0$ as expected. We begin by expanding the Monod function,

$$\begin{aligned} \frac{c_i}{c_i + K} &\approx \frac{c_i}{K} - \left(\frac{c_i}{K}\right)^2 \quad (\text{D2}) \\ &\approx \left(\frac{\phi c_i^{(1)} + \phi^2 c_i^{(2)} + \dots}{K}\right) - \left(\frac{\phi c_i^{(1)} + \phi^2 c_i^{(2)} + \dots}{K}\right)^2 \\ &\approx \phi \left(\frac{c_i^{(1)}}{K}\right) + \phi^2 \left(\left(\frac{c_i^{(2)}}{K}\right) - \left(\frac{c_i^{(1)}}{K}\right)^2\right) + O(\phi^3). \end{aligned}$$

Accordingly, in the kinetic equation for c_i ,

$$\dot{c}_i = -\frac{c_i}{K + c_i} \sum_\sigma \alpha_{\sigma, i} \rho_\sigma, \quad (\text{D3})$$

substituting the expansion in Eq. D2 and keeping the leading order, $c_i^{(1)}$, gives,

$$\begin{aligned} \dot{c}_i^{(1)} &= -c_i^{(1)} \underbrace{\sum_\sigma \frac{\alpha_{\sigma, i} \rho_\sigma(0)}{K}}_{\gamma_i} \quad (\text{D4}) \\ \implies c_i^{(1)} &= c_i^{(1)}(0) e^{-\gamma_i t}. \end{aligned}$$

We next solve for $\rho_\sigma^{(1)}$ using $c_i^{(1)}$, and then we will use $\rho_\sigma^{(1)}$ to solve for $c_i^{(2)}$. It is possible but not necessary for our purposes to iterate further. The kinetic equation for the biomass density ρ_σ is,

$$\dot{\rho}_\sigma = \rho_\sigma \sum_i \alpha_{\sigma, i} \frac{c_i}{K + c_i}. \quad (\text{D5})$$

Substituting the ϕ expansion gives, to leading order,

$$\begin{aligned}\dot{\rho}_\sigma^{(1)} &= \rho_\sigma(0) \sum_i \frac{\alpha_{\sigma,i} c_i^{(1)}}{K} \\ &= \rho_\sigma(0) \sum_i \frac{\alpha_{\sigma,i} c_i^{(1)}(0) e^{-\gamma_i t}}{K} \\ \Rightarrow \rho_\sigma^{(1)} &= \rho_\sigma(0) \sum_i \frac{\alpha_{\sigma,i} c_i^{(1)}(0)}{K \gamma_i} (1 - e^{-\gamma_i t}).\end{aligned}\quad (\text{D6})$$

Taking the long-time limit, $t \gg \frac{1}{\gamma_i}$, we obtain,

$$\rho_\sigma^{(1)}(t \gg \gamma_i^{-1}) = \rho_\sigma(0) \sum_i \frac{\alpha_{\sigma,i} c_i^{(1)}(0)}{K \gamma_i}. \quad (\text{D7})$$

Focusing on the leading order, we conclude that,

$$\rho_\sigma(t \gg \gamma_i^{-1}) = \rho_\sigma(0) + \phi \rho_\sigma(0) \sum_i \frac{\alpha_{\sigma,i} c_i^{(1)}(0)}{K \gamma_i}. \quad (\text{D8})$$

Substituting for γ_i and for $c_i^{(1)}(0) = c_i(0)/\phi$, we have,

$$\rho_\sigma(t \gg \gamma_i^{-1}) \approx \rho_\sigma(0) + \rho_\sigma(0) \sum_i \frac{\alpha_{\sigma,i} c_i(0)}{\sum_{\sigma'} \alpha_{\sigma',i} \rho_{\sigma'}(0)}. \quad (\text{D9})$$

Explicitly stating the batch number d , at the end of the batch, i.e. at time $t = t_f \gg \gamma_i^{-1}$, the biomass density is,

$$\rho_\sigma(d, t_f) \approx \left(1 + \sum_i \frac{\alpha_{\sigma,i} c_i(0)}{\sum_{\sigma'} \alpha_{\sigma',i} \rho_{\sigma'}(d, 0)} \right) \rho_\sigma(d, 0). \quad (\text{D10})$$

In the serial dilution model with complete consumption of all nutrients c_0 and initial biomass ρ_0 , the inoculum populations in batch $d + 1$ can be computed from the populations at the time of complete nutrient consumption, t_f , in batch d ,

$$\begin{aligned}\rho_\sigma(d+1, 0) &= \frac{\rho_0}{\rho_0 + c_0} \rho_\sigma(d, t_f) = \frac{\rho_\sigma(d, t_f)}{1 + c_0/\rho_0} \\ &= \frac{\rho_\sigma(d, 0)}{1 + c_0/\rho_0} \left(1 + \sum_i \frac{\alpha_{\sigma,i} c_i(0)}{\sum_{\sigma'} \alpha_{\sigma',i} \rho_{\sigma'}(d, 0)} \right).\end{aligned}\quad (\text{D11})$$

At steady state, we require that $\rho_\sigma(d+1, 0) = \rho_\sigma(d, 0)$:

$$1 + c_0/\rho_0 = 1 + \sum_i \frac{\alpha_{\sigma,i} c_i(0)}{\sum_{\sigma'} \alpha_{\sigma',i} \rho_{\sigma'}(d, 0)}. \quad (\text{D12})$$

Our calculation, to order ϕ , gives,

$$\frac{c_0}{\rho_0} = \sum_i \frac{\alpha_{\sigma,i} c_i(0)}{\sum_{\sigma'} \alpha_{\sigma',i} \rho_{\sigma'}(0)}. \quad (\text{D13})$$

Dividing both sides by t_f and defining,

$$\delta = \frac{c_0}{\rho_0 t_f}, \quad s_i = \frac{c_i(0)}{t_f}, \quad (\text{D14})$$

we finally reach the $c_0/K \ll 1$ steady-state condition for the serial dilution system:

$$\delta = \sum_i \frac{\alpha_{\sigma,i} s_i}{\sum_{\sigma'} \alpha_{\sigma',i} \rho_{\sigma'}(0)}. \quad (\text{D15})$$

Averaged over a batch, s_i is the average rate that nutrient i is supplied, and δ is the average rate that all the nutrients are supplied per unit inoculum biomass. If this were a chemostat rather than a serial dilution model, then one could think of s_i as the rate nutrient i is continuously supplied. Moreover, for a chemostat, δ , which would be the rate all nutrients are continuously supplied per unit biomass, would need to equal the dilution rate of the chemostat to maintain steady state. Indeed, Eq. D15 is precisely the steady-state condition for the chemostat (Eq. 4 from Ref. [34]) with s_i and δ interpreted as above.

Thus we complete the proof that in $c_0/K \ll 1$, the steady state of our serial dilution model is identical to the steady state of the equivalent chemostat model.

Second-order corrections to remapping of the coexistence boundaries for $c_0/K \ll 1$

We have demonstrated above that the leading terms in an expansion for small nutrient supply retrieve the steady-state solution of the chemostat model. However, we know from numerical simulations, that as $c_0/K \equiv \phi$ is increased, the coexistence boundaries become *remapped*, away from the enzyme strategies. Since there is no remapping at the chemostat limit, equivalent to an expansion to order ϕ as proved above, to capture the remapping we expand to order ϕ^2 in $c_i(t)$. To this end, we return to the ϕ expansion and extract the ϕ^2 contribution,

$$\frac{\dot{c}_i^{(2)}}{K} = \left(\frac{c_i^{(1)}}{K} \right)^2 \gamma_i - \left(\frac{c_i^{(2)}}{K} \right) \gamma_i - \left(\frac{c_i^{(1)}}{K} \right) \sum_\sigma \frac{\alpha_{\sigma,i} \rho_\sigma^{(1)}}{K}. \quad (\text{D16})$$

which gives,

$$\frac{c_i^{(2)}}{K} = \left(\frac{c_i^{(1)}(0)}{K} \right)^2 (e^{-\gamma_i t} - e^{-2\gamma_i t}) - \frac{c_i^{(1)}(0)}{K} \sum_{\sigma} \frac{\alpha_{\sigma,i} \rho_{\sigma}(0)}{K} \sum_j \frac{\alpha_{\sigma,j} c_j^{(1)}(0)}{K \gamma_j} \left(t e^{-\gamma_i t} - \frac{e^{-\gamma_i t} - e^{-(\gamma_i + \gamma_j)t}}{\gamma_j} \right). \quad (\text{D17})$$

Now we can solve for the growth-function integrals I_i for the case of a single species growing in isolation. We expand the growth-function integral,

$$I_i = \int_0^{\infty} \frac{c_i(t')}{c_i(t') + K} dt' = \phi I_i^{(1)} + \phi^2 I_i^{(2)} + \dots \quad (\text{D18})$$

Substituting the order ϕ from Eq. D5 and integrating, gives:

$$I_i^{(1)} = \int_0^{\infty} \frac{c_i^{(1)}(t')}{K} dt' = \frac{c_i^{(1)}(0)}{K \gamma_i}. \quad (\text{D19})$$

For a single species growing in isolation, $\gamma_i = \frac{1}{K} \alpha_{\sigma,i} \rho_{\sigma}(0)$. Thus, to order ϕ , the chemostat limit, we obtain, (in the

chemostat limit, for a single species),

$$I_i = \phi I_i^{(1)} = \frac{c_i(0)}{\alpha_{\sigma,i} \rho_{\sigma}(0)}. \quad (\text{D20})$$

Thus, to satisfy the coexistence boundary conditions: $\forall i : I_i = \text{const}$, to order ϕ it must be that $\forall i : c_i(0)/\alpha_{\sigma,i} = \text{const}$. This is precisely the coexistence condition for the chemostat, explained in Appendix C. To obtain the *remapping* of the coexistence boundaries, we must expand I_i to order ϕ^2 .

To order ϕ^2 we substitute Eq. D5 for $c_i^{(1)}$ and Eq. D17 for $c_i^{(2)}$ and integrate, giving:

$$I_i^{(2)} = \int_0^{\infty} \left[\frac{c_i^{(2)}}{K} - \left(\frac{c_i^{(1)}}{K} \right)^2 \right] dt' = -\frac{c_i^{(1)}(0)}{K} \sum_{\sigma} \frac{\alpha_{\sigma,i} \rho_{\sigma}(0)}{K} \sum_j \frac{\alpha_{\sigma,j} c_j^{(1)}(0)}{\gamma_j K} \left(\frac{1}{\gamma_i^2} - \frac{1}{\gamma_i \gamma_j} + \frac{1}{\gamma_j(\gamma_i + \gamma_j)} \right), \quad (\text{D21})$$

which upon substituting γ_i for a single species simplifies to:

$$\begin{aligned} \phi^2 I_i^{(2)} &= -\frac{c_i(0)}{\rho_{\sigma}(0) \alpha_{\sigma,i}} \sum_j \frac{c_j(0)}{\rho_{\sigma}(0) \alpha_{\sigma,j}} \frac{\alpha_{\sigma,j}^2}{\alpha_{\sigma,i} + \alpha_{\sigma,j}} \quad (\text{D22}) \\ &= -\phi I_i^{(1)} \sum_j \phi I_j^{(1)} \frac{\alpha_{\sigma,j}^2}{\alpha_{\sigma,i} + \alpha_{\sigma,j}}. \end{aligned}$$

Collecting terms to order ϕ^2 gives

$$I_i = \phi I_i^{(1)} \left(1 - \sum_j \phi I_j^{(1)} \frac{\alpha_{\sigma,j}^2}{\alpha_{\sigma,i} + \alpha_{\sigma,j}} \right) + O(\phi^3). \quad (\text{D23})$$

As before, the coexistence boundaries are defined by $I_i = \text{const}$. To order ϕ^2 , Eq. D23 can be used to solve for this remapping analytically. Eq. D23 also clarifies why perfect generalists ($\forall i, j : \alpha_{\sigma,i} = \alpha_{\sigma,j}$) do not get remapped, as stated in the main text. This is because for a generalist $\forall i, j : \alpha_{\sigma,j}^2 / (\alpha_{\sigma,i} + \alpha_{\sigma,j}) = \text{const.}$, meaning that the second-order I_i will all be equal if the first-order I_i are all the same. Moreover, the term $I_j^{(1)} \propto \rho_{\sigma}^{-1}(0)$ multiplies the order ϕ^2 correction to the coexistence boundary, and as a result, the larger $\rho_{\sigma}(0)$, the smaller the remapping. A comparison between the analytic form of the remapping at small c_0/K and its numerical form is shown below. As is apparent, the agreement is

excellent and extends to higher c_0/K as ρ_0/K increases because at high ρ_0/K the remapping is small.

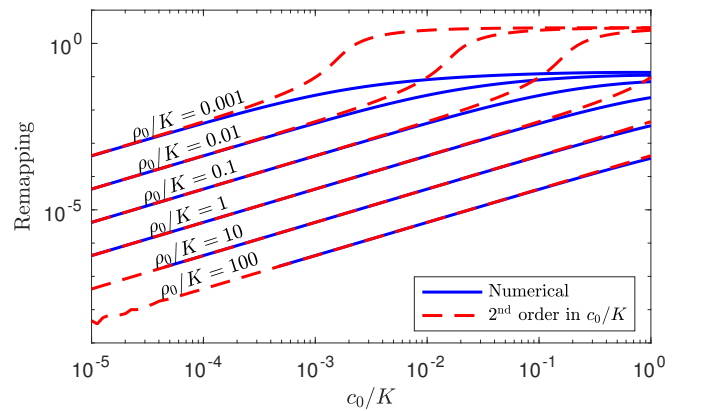


FIG. 7: Numerical solution and analytical perturbation theory results for remapping of the coexistence boundaries at low c_0 . The analytic solution is derived from $\forall i : I_i = \text{const}$ using the second-order expansion in Eq. D23.

Appendix E: Remapping of the coexistence boundaries for $c_0/K \gg 1$

Here we show that at high c_0/K the coexistence boundaries remap to their chemostat positions. When a large nutrient bolus is present, the growth function is effectively always saturated such that

$$\frac{d\rho_\sigma}{dt} = \rho_\sigma \sum_{i=1}^p \alpha_{\sigma,i} \frac{c_i}{K + c_i} \approx \rho_\sigma \sum_i \alpha_{\sigma,i} = \rho_\sigma E, \quad (\text{E1})$$

where $\sum_i \alpha_{\sigma,i} = E$ is in units of 1/time, without loss of generality E can be set to unity, but we keep it here to make the units explicit. Solving for $\rho(t)$ yields $\rho(t) = \rho_0 e^{Et}$. The assumption that $c_i \gg K$ can then be applied to the nutrient dynamics, yielding:

$$\frac{dc_i}{dt} = -\alpha_{\sigma,i} \rho_\sigma(t) \frac{c_i}{K + c_i} \approx -\alpha_{\sigma,i} \rho_0 e^{Et}. \quad (\text{E2})$$

Solving for the nutrient dynamics leads to $c_i(t) = c_i(0) + \frac{\alpha_{\sigma,i}}{E} \rho_0 (1 - e^{Et})$. Since the growth function is nearly always saturated (giving an integrand value of 1), the growth-function integral $I_i = \int_0^\infty \frac{c_i}{K_i + c_i} dt$ approximately equals the time of nutrient exhaustion. Thus for a given nutrient i , the time when that nutrient is depleted $t_{i,f}$ is given by:

$$t_{i,f} = I_i = \frac{1}{E} \ln \left(1 + \frac{c_i(0)E}{\alpha_{\sigma,i} \rho_0} \right). \quad (\text{E3})$$

Note that the coexistence boundaries are defined by $\forall i : I_i = \text{const}$ which is satisfied when the fraction of nutrients in the initial bolus matches the strategies,

$$\forall i : c_i(0)/\alpha_{\sigma,i} = \text{const}. \quad (\text{E4})$$

This is precisely the result in Appendix C, indicating that in the $c_0/K \gg 1$ limit the coexistence boundaries return to their chemostat values.

Appendix F: Supplemental Figures

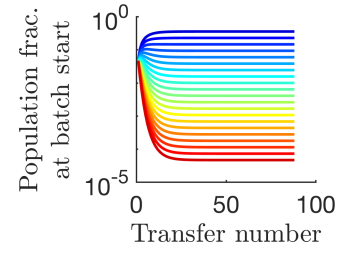


FIG. 8: Serial dilution model with unequal Y_i and K_i . In the main text, we assume that all nutrients are equally valuable ($Y_i \equiv Y$) and equally accessible ($K_i \equiv K$). Here we show that relaxing these assumptions still allows unlimited species coexistence as long as all species have the same Y_i and K_i for a given nutrient. In the simulation shown, $K_1 = 10$, $K_2 = 3$, $Y_1 = 2$, and $Y_2 = 5$. The 21 strategies are equally spaced, with equal initial inocula, Nutrient 1 fraction 0.3, and $\rho_0 = c_0 = 1$.

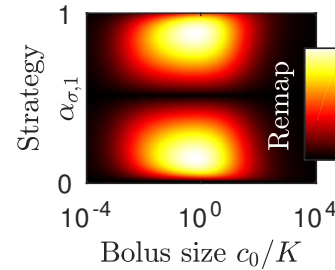


FIG. 9: Dependence of coexistence boundary remapping on c_0/K . As a further exposition to Fig. 3A in the main text, shown here is the difference between the remapped coexistence boundaries and the corresponding metabolic strategies as a function of c_0/K and metabolic strategy.

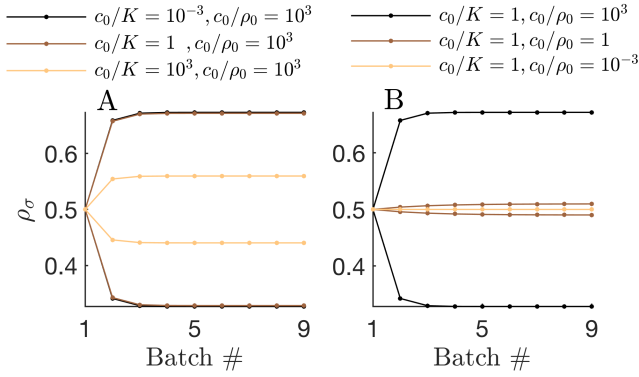


FIG. 10: Batch timecourses of a bitrophic model with only two species. To further investigate the difference between the unitrophic and bitrophic scenarios, we consider a toy system with only two species, Species 1 with strategy (0.05, 0.95) and Species 2 with strategy (0.95, 0.05). We set the byproduct matrix for perfect conversion, and the nutrient bolus composition so that only Nutrient 2 is provided. By the end of each batch, the same amounts of Nutrient 1 and Nutrient 2 have been consumed. (A) Simulations with constant c_0/ρ_0 and variable c_0/K . The “early-bird” effect becomes stronger with decreasing c_0/K , since this allows the dominant species to grow more before the byproduct can be readily consumed. (B) Simulations with variable c_0/ρ_0 and constant c_0/K . The “early-bird” effect is stronger at higher c_0/ρ_0 because the larger amount of supplied nutrient allows the dominant species to build a large population which can then out-compete other species. Conversely, if instead of cross-feeding we were to supply in the nutrient bolus equal quantities of Nutrients 1 and 2, the result would be equal abundance of both species.

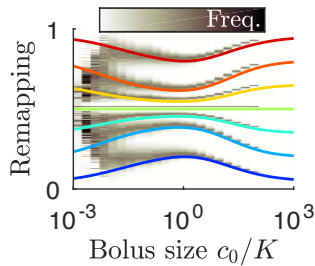


FIG. 11: Remapping under stochastic Gillespie dynamics without mutation ($\nu = 0$). With stochastic growth dynamics, the remapping itself becomes stochastic with a large variance for $c_0/K \ll 1$. For every observation of remapping at a given strategy and c_0/K value, the growth-function integrals I_i were computed across the range of nutrient supply proportions. The remapped coexistence boundary for that set of simulations is the nutrient supply which produced the smallest difference between I_1 and I_2 . For a given strategy and c_0/K value, this procedure was repeated multiple times to obtain a remapping density. Here, the log of the remapping density is shown as a heatmap for $\rho_0/K = 10^{-3}$. Colored curves show the corresponding deterministic remapping from Fig. 3A in the main text.

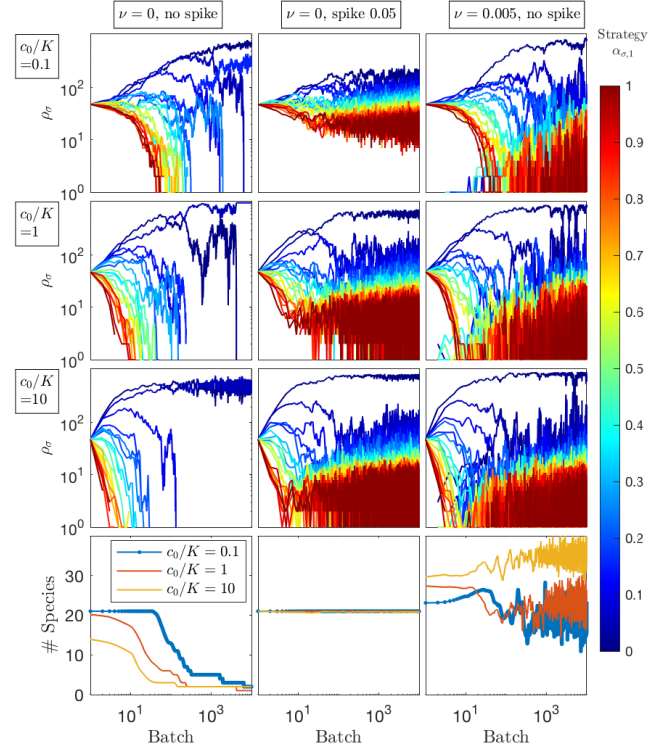


FIG. 12: Timecourses of three stochastic models: no mutation or spike-in, only spike-in, and only mutation. In the main text, we only present data on the steady states of the stochastic models while here we examine the full timecourses. In all cases, inter-batch sampling is stochastic without replacement. In the model without mutations ($\nu = 0$) and without spike-in, sampling causes extinctions of species with no possibility of recovery. The model with no mutations but with spike-in results in the number of species stabilizing at steady state. The model with mutations but without spike-in results in a fluctuating number of species, as species constantly go extinct and are reborn through mutation. x -axis is batch number.

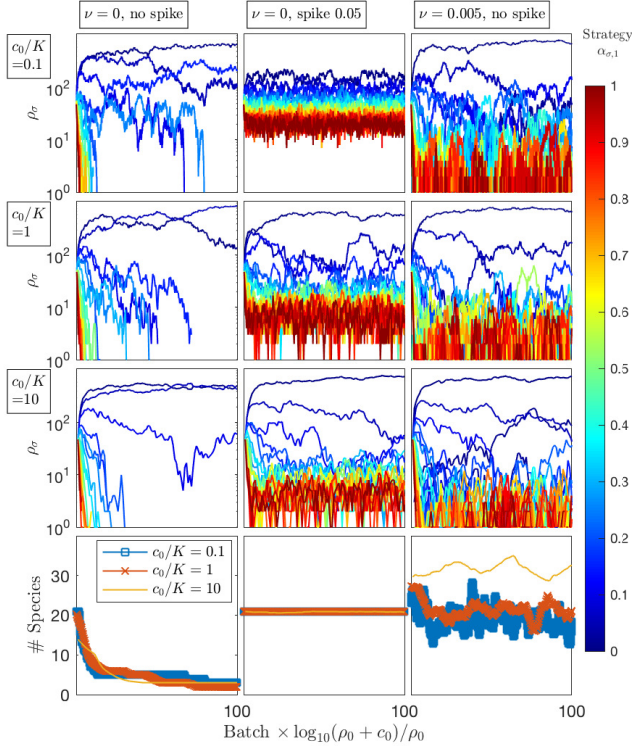


FIG. 13: Timecourses of three stochastic models, as in Fig. 12, but rescaling the x -axis to approximate true time. We scale the number of batches by the time it takes to consume c_0 nutrients as $\log\left(\frac{\rho_0 + c_0}{\rho_0}\right)$. This approximation comes from assuming saturated growth dynamics ($\rho(t) = \rho_0 e^{Et}$) and computing the time it takes to consume c_0 nutrients.

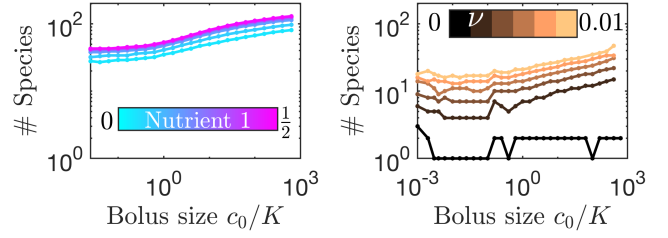


FIG. 14: *Left*: Number of extant species under mutation-selection balance. Complementing Fig. 5 in the main text, here we present the median number of extant species vs. c_0/K for varying supply proportions with $\nu = 0.01$, $\rho_0 = 1000$, and $K = 1000$. The number of species is recorded at the beginning of each batch. As c_0/K increases, the number of extant species (species with non-zero abundance) increases due to more opportunities for mutations. More evenly balanced nutrient supplies lead to a larger number of species. *Right*: Median number of extant species as a function of c_0/K at different mutation rates ν from 0 (black) to 0.01 (orange) with supply composition (0.005, 0.995). With increasing ν , more species are created by mutation during each batch. When $\nu = 0$, the median number of extant species fluctuates between one and two species due to extinctions through sampling noise. When $\nu > 0$, the steady state reflects a balance between the addition of new species through mutation and the loss of species due to inter-batch sampling.

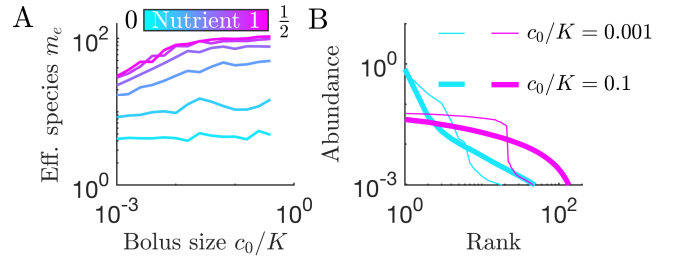


FIG. 15: Mutation-selection balance for high ρ_0 and K ($\rho_0 = 10^5$, $K = 10^5$, and $\nu = 10^{-3}$). The results presented in Fig. 5 in the main text are for $\rho_0 = 1000$, $K = 1000$, and $\nu = 0.01$. With these parameters, sampling noise dominates in the $c_0/K \ll 1$ limit. Here, we explore the $c_0/K \ll 1$ limit using larger ρ_0 and K . (A) Effective number of species m_e for different nutrient compositions (colors) as a function of nutrient bolus size c_0/K . (B) Rank-abundance curves for Nutrient 1 fraction 0.05 (cyan) and 0.5 (magenta); line thickness corresponds to c_0/K values. We note the similar trends to the results in the main text, with a sharper decrease in the rank-abundance curves for $c_0/K \ll 1$, a regime difficult to characterize for $K = 1000$ as it is dominated by sampling noise.

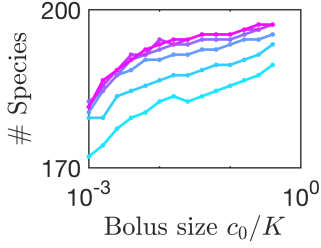


FIG. 16: Number of extant species under mutation-selection balance for $\rho_0 = 10^5$, $K = 10^5$, and $\nu = 10^{-3}$. Note the monotonic increase in the median number of extant species with c_0 without saturating the total number of possible species (here 201).

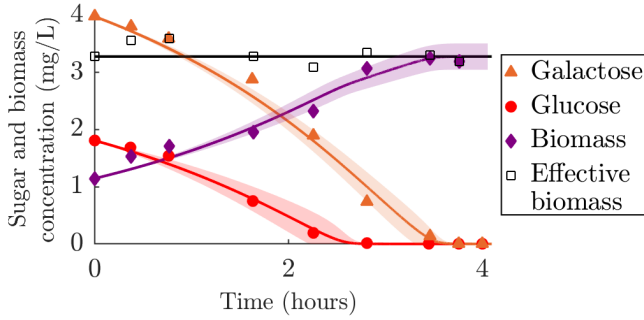


FIG. 17: Comparison of serial dilution model fit to batch growth data from Lendenmann et al. [52]. This data is similar to that in Fig. 6C, except that the inoculum was taken from galactose-limited conditions instead of glucose limited conditions. Solid curves are model predictions and the shaded area is the 95% prediction bound (see Appendix A for details). “Effective biomass” refers to the total biomass within the system: $M(t) = \rho(t) + Y(c_1(t) + c_2(t))$. Since the data for the three timeseries were measured at slightly different times, the effective for the experimental data was obtained by linear interpolation of the data points. The inferred parameters were the strategy (α_1, α_2) for the two sugars, glucose and galactose, and the yield Y . The estimated α_i , measured in units of $(\text{mg sugar})(\text{mg biomass})^{-1}\text{h}^{-1}$, were 0.43 ± 0.06 and 0.57 ± 0.04 for glucose and galactose, respectively. The estimated yield of $0.37 \pm 0.03 (\text{mg biomass})(\text{mg sugar})^{-1}$ was similar to that inferred in Fig. 6C.

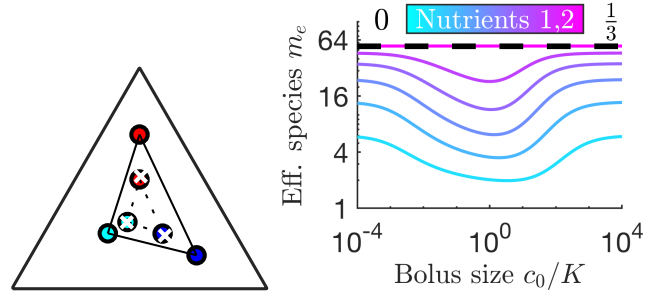


FIG. 18: Serial dilution model with three nutrients. *Left*: Example of remapping on the three nutrient simplex, similar to Fig. 2 from the main text. Here we show how the remapping analysis presented in the main text for two nutrients can be extended to three nutrients. Remapping of three strategies for $c_0/K = 1$ and $\rho_0 = 10^{-2}$. Outer circles: strategies $\{\vec{\alpha}_\sigma\}$; inner circles: remapped nodes; white X’s: remapped nodes from stochastic dynamics as in Fig. 11; lines connecting outer circles: supplies within this convex hull of strategies lead to coexistence of all species in the chemostat regime $c_0/K \ll 1$; dashes connecting inner circles: approximate remapped convex hull boundary defining region of supplies leading to coexistence for $c_0/K = 1$. Note that, as in the two nutrient case, the strategies map inwards on the simplex for $c_0/K \approx 1$. *Right*: Steady-state effective number of species m_e versus c_0/K for equal initial inocula of 64 species equally spaced throughout the triangular simplex competing for three nutrients. Effective number of species shows the same trend of loss in diversity when $c_0/K \approx 1$ as in the two nutrient case in Fig. 3C.

- [1] R. Daniel, The metagenomics of soil, *Nature Reviews Microbiology* **3**, 470 (2005).
- [2] J. Lloyd-Price, G. Abu-Ali, and C. Huttenhower, The healthy human microbiome, *Genome Medicine* **8**, 51 (2016).
- [3] S. A. Levin, Community Equilibria and Stability, and an Extension of the Competitive Exclusion Principle, *Am. Nat.* **104**, 413 (1970).
- [4] R. A. Armstrong and R. McGehee, Competitive Exclusion, *Am. Nat.* **115**, 151 (1980).
- [5] G. E. Hutchinson, The paradox of the plankton, *Am. Nat.* **95**, 137 (1961).
- [6] R. Ptacnik, A. G. Solimini, T. Andersen, T. Tamminen, P. Bretum, L. Lepisto, E. Willen, and S. Rekolainen, Diversity predicts stability and resource use efficiency in natural phytoplankton communities, *Proc. Natl. Acad. Sci. U.S.A.* **105**, 5134 (2008).
- [7] J. D. van Elsas, M. Chiurazzi, C. A. Mallon, D. Elhottova, V. Kristufek, and J. F. Salles, Microbial diversity determines the invasion of soil by a bacterial pathogen, *Proc. Natl. Acad. Sci. U.S.A.* **109**, 1159 (2012).
- [8] Y. Taur, R. R. Jenq, M. A. Perales, E. R. Littmann, S. Morjaria, L. Ling, D. No, A. Gouborne, A. Viale, P. B. Dahi, D. M. Ponce, J. N. Barker, S. Giralt, M. Van Den Brink, and E. G. Pamer, The effects of intestinal tract bacterial diversity on mortality following allogeneic hematopoietic stem cell transplantation, *Blood* **124**, 1174 (2014).
- [9] R. R. Stein, V. Bucci, N. C. Toussaint, C. G. Buffie, G. Rtsch, E. G. Pamer, C. Sander, and J. B. Xavier, Ecological modeling from time-series inference: Insight into dynamics and stability of intestinal microbiota, *PLoS Computational Biology* **9**, e1003388 (2013).
- [10] A. Goyal and S. Maslov, Diversity, Stability, and Reproducibility in Stochastically Assembled Microbial Ecosystems, *Physical Review Letters* **120**, 158102 (2018), arXiv:1711.00755 .
- [11] E. D. Kelsic, J. Zhao, K. Vetsigian, and R. Kishony, Counteraction of antibiotic production and degradation stabilizes microbial communities, *Nature* **521**, 516 (2015), arXiv:15334406 .
- [12] J. Huisman, P. van Oostveen, and F. J. Weissing, Species Dynamics in Phytoplankton Blooms: Incomplete Mixing and Competition for Light, *Am. Nat.* **154**, 46 (1999).
- [13] B. Momeni, K. A. Brileya, M. W. Fields, and W. Shou, Strong inter-population cooperation leads to partner intermixing in microbial communities, *eLife* **2**, e00230 (2013).
- [14] T. F. Thingstad, Elements of a theory for the mechanisms controlling abundance, diversity, and biogeochemical role of lytic bacterial viruses in aquatic systems, *Limnology and Oceanography* **45**, 1320 (2000).
- [15] M. W. Palmer, Variation in species richness: Towards a unification of hypotheses, *Folia Geobotanica et Phytotaxonomica* **29**, 511 (1994).
- [16] F. H. Chang, J. Zeldis, M. Gall, and J. Hall, Seasonal and spatial variation of phytoplankton assemblages, biomass and cell size from spring to summer across the north-eastern New Zealand continental shelf, *Journal of Plankton Research* **25**, 737 (2003).
- [17] S. A. Smits, J. Leach, E. D. Sonnenburg, C. G. Gonzalez, J. S. Lichtman, G. Reid, R. Knight, A. Manjurano, J. Changanlucha, J. E. Elias, M. G. Dominguez-Bello, and J. L. Sonnenburg, Seasonal cycling in the gut microbiome of the hadza hunter-gatherers of tanzania, *Science* **357**, 802 (2017).
- [18] R. Lenski and M. Travisano, Dynamics of Adaptation and Diversification, *Proc. Natl. Acad. Sci. U.S.A.* **91**, 6808 (1994).
- [19] J. E. Goldford, N. Lu, D. Baji, S. Estrela, M. Tikhonov, A. Sanchez-Gorostiaga, D. Segr, P. Mehta, and A. Sanchez, Emergent simplicity in microbial community assembly, *Science* **361**, 469 (2018).
- [20] E. A. Yurtsev, A. Conwill, and J. Gore, Oscillatory dynamics in a bacterial cross-protection mutualism, *Proc. Natl. Acad. Sci. U.S.A.* **113**, 6236 (2016), arXiv:arXiv:1408.1149 .
- [21] F. M. Stewart and B. R. Levin, Partitioning of Resources and the Outcome of Interspecific Competition : A Model and Some General Considerations, *Am. Nat.* **107**, 171 (1973).
- [22] H. L. Smith, Bacterial competition in serial transfer culture, *Math. Biosci.* **229**, 149 (2011).
- [23] D. Tilman, *Resource Competition and Community Structure* (Princeton U. Press, 1982).
- [24] P. A. Abrams, Monotonic or Unimodal Diversity-Productivity Gradients: What Does Competition Theory Predict?, *Ecology* **76**, 2019 (1995).
- [25] M. A. Leibold, A Graphical Model of Keystone Predators in Food Webs: Trophic Regulation of Abundance, Incidence, and Diversity Patterns in Communities, *Am. Nat.* **147**, 784 (1996).
- [26] G. G. Mittelbach, C. F. Steiner, S. M. Scheiner, K. L. Gross, H. L. Reynolds, R. B. Waide, M. R. Willig, S. I. Dodson, and L. Gough, What is the observed relationship between species richness and productivity?, *Ecology* **82**, 2381 (2001).
- [27] R. B. Waide, M. R. Willig, and C. F. Steiner, The relationship between productivity and species richness, *Annual Review of Ecology and Systematics* **30**, 257 (1999).
- [28] P. B. Adler, E. W. Seabloom, E. T. Borer, H. Hillebrand, Y. Hautier, A. Hector, W. S. Harpole, L. R. O'Halloran, J. B. Grace, T. M. Anderson, *et al.*, Productivity is a poor predictor of plant species richness, *Science* **333**, 1750 (2011).
- [29] C. Bienhold, A. Boetius, and A. Ramette, The energy-diversity relationship of complex bacterial communities in arctic deep-sea sediments, *The ISME Journal* **6**, 724 (2012).
- [30] H. C. Bernstein, C. Brislawn, R. S. Renslow, K. Dana, B. Morton, S. R. Lindemann, H.-S. Song, E. Atci, H. Beyenal, J. K. Fredrickson, J. K. Jansson, and J. J. Moran, Trade-offs between microbiome diversity and productivity in a stratified microbial mat, *The ISME Journal* **11**, 405 (2016).
- [31] R. Kassen, A. Buckling, G. Bell, and P. B. Ralney, Diversity peaks at intermediate productivity in a laboratory microcosm, *Nature* **406**, 508 (2000).
- [32] V. H. Smith, Microbial diversity-productivity relationships in aquatic ecosystems, *FEMS Microbiology Ecology* **62**, 181 (2007).
- [33] K. Kovárová-Kovar and T. Egli, Growth kinetics of suspended microbial cells: From single-substrate-controlled growth to mixed-substrate kinetics, *Microbiology and Molecular Biology Reviews* **62**, 646 (1998).
- [34] A. Posfai, T. Taillefumier, and N. S. Wingreen, Metabolic trade-offs promote diversity in a model ecosystem, *Phys. Rev. Lett.* **118**, 028103 (2017).
- [35] M. L. Rosenzweig, Paradox of Enrichment : Destabilization of Exploitation Ecosystems in Ecological Time, *Science* **171**, 385 (1971).
- [36] L. Jost, Entropy and diversity, *Oikos* **113**, 363 (2006).
- [37] S. Abel, P. Abel zur Wiesch, B. M. Davis, and M. K. Waldor, Analysis of bottlenecks in experimental models of infection, *PLoS Pathogens* **11**, e1004823 (2015).
- [38] R. H. MacArthur and E. O. Wilson, *The Theory of Island Bio-*

- geography* (Princeton U. Press, 2001).
- [39] B. H. Good, S. Martis, and O. Hallatschek, Adaptation limits ecological diversification and promotes ecological tinkering during the competition for substitutable resources, *Proc Natl Acad Sci USA* **115**, E10407 (2018).
- [40] J. Monod, *Recherches sur la croissance des cultures bactériennes* (Hermann and Cie, 1942).
- [41] U. Münster, Concentrations and fluxes of organic carbon substrates in the aquatic environment, *Antonie van Leeuwenhoek* **63**, 243 (1993).
- [42] T. Egli, U. Lendenmann, and M. Snozzi, Kinetics of microbial growth with mixtures of carbon sources, *Antonie van Leeuwenhoek* **63**, 289 (1993).
- [43] U. Lendenmann, M. Snozzi, and T. Egli, Kinetics of the simultaneous utilization of sugar mixtures by *Escherichia coli* in continuous culture, *Appl. Environ. Microbiol.* **62**, 1493 (1996).
- [44] U. Lendenmann and T. Egli, Kinetic models for the growth of *Escherichia coli* with mixtures of sugars under carbon-limited conditions, *Biotechnology and Bioengineering* **59**, 99 (1998).
- [45] J.-H. Kim, S. P. Shoemaker, and D. A. Mills, Relaxed control of sugar utilization in *Lactobacillus brevis*, *Microbiology* **155**, 1351 (2009).
- [46] P. Scherer and H. Sahm, Influence of sulphur-containing compounds on the growth of *Methanosarcina barkeri* in a defined medium, *European journal of applied microbiology and biotechnology* **12**, 28 (1981).
- [47] M. Scott, C. W. Gunderson, E. M. Mateescu, Z. Zhang, and T. Hwa, Interdependence of cell growth and gene expression: Origins and consequences, *Science* **330**, 1099 (2010).
- [48] M. Basan, S. Hui, H. Okano, Z. Zhang, Y. Shen, J. R. Williamson, and T. Hwa, Overflow metabolism in *Escherichia coli* results from efficient proteome allocation, *Nature* **528**, 99 (2015).
- [49] M. T. Wortel, E. Noor, M. Ferris, F. J. Bruggeman, and W. Liebermeister, Metabolic enzyme cost explains variable trade-offs between microbial growth rate and yield, *PLoS Computational Biology* **14**, 1 (2018).
- [50] L. Aldén, F. Demoling, and E. Bååth, Rapid method of determining factors limiting bacterial growth in soil, *Applied and Environmental Microbiology* **67**, 1830 (2001).
- [51] F. Demoling, D. Figueroa, and E. Bth, Comparison of factors limiting bacterial growth in different soils, *Soil Biology and Biochemistry* **39**, 2485 (2007).
- [52] U. Lendenmann, H. Senn, M. Snozzi, and T. Egli, Dynamics of mixed substrate growth of *Escherichia coli* in batch culture: the transition between simultaneous and sequential utilisation of carbon substrates, *Acta Universitatis Carolinae Environmentalica* **14**, 21 (2000).